MISSOURI S&T

Missouri University of Science and Technology

Scholars' Mine

Mechanical and Aerospace Engineering Faculty Research & Creative Works

Mechanical and Aerospace Engineering

01 Sep 2009

Phase Change Mechanisms During Femtosecond Laser Pulse Train Ablation of Nickel Thin Films

Xin Li

Lan Jiang
Missouri University of Science and Technology, jianglan@mst.edu

Hai-Lung Tsai
Missouri University of Science and Technology, tsai@mst.edu

Follow this and additional works at: https://scholarsmine.mst.edu/mec_aereng_facwork

Part of the Aerospace Engineering Commons, and the Mechanical Engineering Commons

Recommended Citation

X. Li et al., "Phase Change Mechanisms During Femtosecond Laser Pulse Train Ablation of Nickel Thin Films," *Journal of Applied Physics*, American Institute of Physics (AIP), Sep 2009.
The definitive version is available at https://doi.org/10.1063/1.3223331

Phase change mechanisms during femtosecond laser pulse train ablation of nickel thin films

Xin Li,[1] Lan Jiang,[1,a)] and Hai-Lung Tsai[2]

[1]*Laser Micro/Nano Fabrication Laboratory, School of Mechanical Engineering, Beijing Institute of Technology, Beijing 100081, People's Republic of China*
[2]*Laser-Based Manufacturing Laboratory, Department of Mechanical and Aerospace Engineering, Missouri University of Science and Technology (formerly University of Missouri-Rolla), Rolla, Missouri 65409, USA*

The mechanisms of nickel thin films irradiated by femtosecond laser pulse trains are studied by a model using molecular dynamics simulations and two-temperature model. It is found that the pulse train technology can change energy transport and corresponding phase change processes. Compared with single pulse ablation at the same total fluence, the pulse trains lead to (1) lower ablation rate with more and smaller uniform nanoparticles, (2) higher film surface temperatures and longer thermalization time, (3) much lower electron thermal conductivity that can further control heat-affected zone, (4) significantly smaller film compressive stresses and tensile stresses which reduce microcracks, and (5) a transition from phase explosion to the critical point phase separation which favors small uniform nanoparticle generation. © *2009 American Institute of Physics.*
[doi:10.1063/1.3223331]

I. INTRODUCTION

A femtosecond laser pulse can fully ionize almost any solid material and greatly reduce recast, microcracks, and heat-affected zone. Hence, femtosecond laser is very promising for the micro-/nanofabrication.[1–4] Recent developments of optical devices make it possible to obtain almost any arbitrary pulse shapes. Many studies have been reported regarding pulse shaping and its effects on laser-material interaction.[5–8] By using pulse train technology, ionization process can be controlled[5] and atoms can be selectively ionized.[6] Such unique abilities of pulse train technology make it promising to improve the quality/precision of micro-/nanofabrication and microanalysis application (such as laser induced breakdown spectroscopy).[7,8]

Semerok and Dutouquet[9] experimentally investigated the ultrashort laser pulse train ablation of aluminum and copper by optical microscope profilometer and observed a decrease in crater depths as pulse separation increased. Noël and Hermann[10] studied the femtosecond laser pulse train ablation of copper and gold by fast imaging and demonstrated that the fraction of atoms in ablation plumes increased whereas the fraction of nanoparticles in ablation plumes decreased. Korte *et al.*[11] studied the femtosecond laser pulse train ablation of chrome by scanning electron microscope and achieved sub-diffraction limited structures. Chen *et al.*[12] explored the femtosecond laser pulse train ablation lithium niobate and found a significant decrease in the ablation threshold as pulse number increased. Vorobyev and Guo[13] studied the femtosecond laser pulse train ablation of gold by laser calorimetry technique and found a significant enhancement in laser light absorption.

Although some preliminary explanations such as plasma reheating and enhanced absorption coefficient were given to explain the results above, a solid theoretical basis for the mechanisms still need to be developed. Jiang and Tsai[14] theoretically studied the ultrashort laser pulse train heating of gold using an improved two-temperature model (TTM) and predicted possible higher photon efficiency. Also, Jiang and Tsai[15] studied the ultrashort laser pulse train ablation of dielectrics using a plasma model and predicted smaller repeatable structures. Huang *et al.*[16] investigated the femtosecond laser pulse train ablation of gold using TTM combined with the phase interface track methods and predicted smaller ablation depth when the second pulse launched at the peak of surface temperature. The theoretical models predicted some phenomena and mechanisms by pulse train technology effectively.

However, the above theoretical models, which do not investigate the detailed phase change mechanisms by pulse train technology, for which molecular dynamics (MD) simulations can be used. Ivanov and Zhigilei[17] studied the ultrashort laser single pulse melting of 50 nm nickel and gold freestanding films and discussed the relative contributions of homogeneous and heterogeneous melting mechanisms. Cheng and Xu[18] studied the femtosecond laser single pulse ablation of 187 nm nickel films and found that phase explosion was responsible for low fluence laser ablation. Wang and Lu[19] studied the picosecond laser single pulse ablation of argon and observed the epitaxial regrowth in the solidification.

This study investigates the femtosecond laser pulse train ablation of 200 nm nickel thin films using a model that combines MD simulations and TTM. Especially the phase change mechanisms for femtosecond laser multiple-pulse trains are carefully explored.

---

a)Author to whom correspondence should be addressed. Tel.: +86-10-6891-4517. Electronic address: jianglan@bit.edu.cn.

106, 064906-1

II. MODEL AND SIMULATION METHOD

TTM treats the electrons and lattices as two separate subsystems, which has been widely used in ultrashort laser processing of metals:[20]

$$C_e(T_e)\frac{\partial T_e}{\partial t} = \nabla(k_e(T_e)\nabla T_e) - G(T_e - T_l) + S(z,t), \quad (1)$$

$$C_l(T_l)\frac{\partial T_l}{\partial t} = G(T_e - T_l), \quad (2)$$

where T_e is the electron temperature, T_l is the lattice temperature, C_e is the electron heat capacity, C_l is the lattice heat capacity, k_e is the electron heat conductivity, and G is the electron-lattice coupling factor. For nickel, this study assumes that $C_e = \gamma T_e$, $\gamma = 1065$ J/m^3 K^2, $C_l = 4.1$ J/kg K, and $k_e = k_0 T_e/T_l$, where $k_0 = 91$ W/m K and $G = 3.6 \times 10^{17}$ W/m^3 K.[21]

20 pulses are imposed on the 200 nm nickel thin films along the z direction with uniform spatial distribution, and the laser source term S is expressed as follows:

$$S(z,t) = \frac{0.94J}{t_p\delta}\sum_{n=1}^{20}\frac{1}{20}\exp\left[-2.77\left(\frac{t-t_{n0}}{t_p}\right)^2\right]\exp\left(-\frac{z-z_{n0}}{\delta}\right), \quad (3)$$

where J is the absorbed total laser fluence, δ is the optical penetration depth, t_p is the pulse duration, t_{n0} is the center of the nth Gaussian pulse, z_{n0} is the position of the dynamic surfaces during the nth Gaussian pulse irradiation, t is the time, and z is the position where the initial film surface is located at $z=0$. In our study, $\delta = 13.5$ nm,[21] and $t_p = 100$ fs. Two cases are considered: (1) $t_{n0} = 1$ ps, referred as the single pulse case; (2) $t_{n0} = n$ ps, referred as the 20 pulses case.

This paper studies $18 \times 2 \times 200$ nm^3 nickel thin films consisting of 673 200 atoms. The interactions among the nickel atoms are described by the Morse potential:[22]

$$\Phi(r_{ij}) = D(e^{-2\alpha(r_{ij}-r_0)} - 2e^{-\alpha(r_{ij}-r_0)}), \quad (4)$$

where $\Phi(r_{ij})$ is the potential energy of two atoms i and j separated by a distance r_{ij}, D is the dissociation energy, α is a constant with dimension of reciprocal distance, and r_0 is the equilibrium distance between two atoms. For nickel, the coefficients are as follows: $D = 0.4205$ eV, $\alpha = 14.199$ nm^{-1}, and $r_0 = 0.278$ nm.[22]

TTM describes the electron heating effectively.[23] MD simulation is a powerful tool to describe the phase change.[19] In the combined model, the MD simulations substitute the TTM for lattice temperature.[17] The lattice heating by the hot electrons is achieved by scaling the atom velocities with a factor[24]

$$\beta = \left[1 + \frac{\Delta t G(T_e - T_l)V}{0.5\sum_{i=1}^{N} m_i[(v_{xi} - \overline{v_x})^2 + (v_{yi} - \overline{v_y})^2 + (v_{zi} - \overline{v_z})^2]}\right]^{1/2}, \quad (5)$$

where v_{xi}, v_{yi}, and v_{zi} are the velocities of atom i in the directions x, y, and z, respectively; $\overline{v_x}$, $\overline{v_y}$, and $\overline{v_z}$ are the average velocities of atom i in the directions x, y, and z, respectively; N is the number of atoms within a layer, V is the volume of the layer, and Δt is the time step. Periodic boundary conditions are imposed in the x, y directions and nonreflecting boundary conditions are imposed in the z direction.[25] Before the laser irradiation, the nickel thin films are equilibrated at 300 K.

III. RESULTS AND DISCUSION

20 pulses at the pulse duration of 100 fs and the total fluence of 0.28 J/cm^2 are investigated in this study. The total laser fluence is slightly above the volumetric phase change threshold fluence of single pulse ablation predicted by Cheng and Xu.[26] It is revealed that the phase change phenomenon in 20 pulse case is different from that in single pulse case, as shown in Fig. 1, in which the first 70 nm film near the surface is shown. In the single pulse case, melting occurs at about 4 ps. During 4–15 ps, the liquid-solid interfaces (melting fronts) move into the nickel films at an average propagation velocity of about 3300 m/s. At 15 ps, the vapor phases appear and expand outside with hundreds of atoms from dynamic film surfaces [Fig. 1(a)]. At 50 ps, several gas bubbles form inside the nickel films at the positions of $z=-10$ nm and $z=-22$ nm where the negative value denotes the position above the initial film surface [Fig. 1(b)]. The bubbles grow rapidly and induce the nickel films to fracture inside. At 92 ps, the nickel films disintegrate into several pieces [Fig. 1(c)]. At 200 ps, several large nanoparticles are created above the dynamic film surfaces and the ablation rate is about 13 nm [Fig. 1(d)]. In the 20 pulse case, melting appears at about 6 ps, that is, phase change occurs during the irradiance of pulse trains. During 6–15 ps, the melting fronts move into the nickel films at an average propagation velocity of about 1800 m/s. At 15 ps, a slow expansion of dynamic film surfaces almost without vapor phases is observed [Fig. 1(e)]. At 50 ps, mixtures of liquid particles and atoms spurt out from dynamic film surfaces [Fig. 1(f)]. Note that no gas bubbles form inside the nickel films. At 92 ps, the nickel films decompose from the uppermost film [Fig. 1(g)]. At 200 ps, a large number of small uniform nanoparticles (1–4 nm) are observed above dynamic film surfaces and the ablation rate is estimated to be 11 nm [Fig. 1(h)]. In general, lower ablation rate, more and smaller uniform nanoparticles are observed in the 20 pulse case. The simulation results of better fabrication precision (lower ablation rate) correspond with previous experimental results,[9,11,27] which demonstrates lower ablation depth by pulse train technology. The simulation results of more and smaller uniform nanoparticle generation correspond with
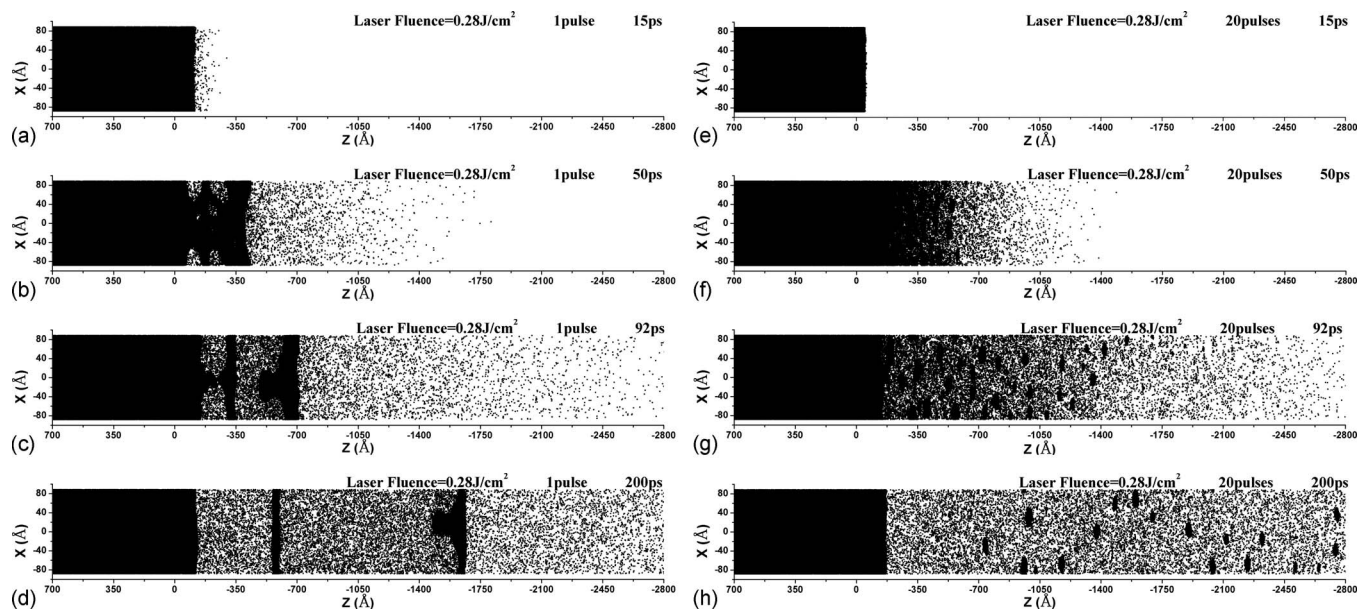
FIG. 1. The snapshots of nickel thin films irradiated by femtosecond laser pulse trains with the total fluence of 0.28 J/cm², where X is in the direction of Ni (100) surface and Z is in the direction of laser irradiance. [(a)–(d)] The single pulse case. [(e)–(h)] The 20 pulse case.

previous experimental results,[10] which demonstrates higher fraction of atoms or small nanoparticles by pulse train technology.

Figure 2 shows the electron and lattice temperatures of the layers next to the dynamic film surfaces. In the single pulse case, the electron temperature is rapidly increased to
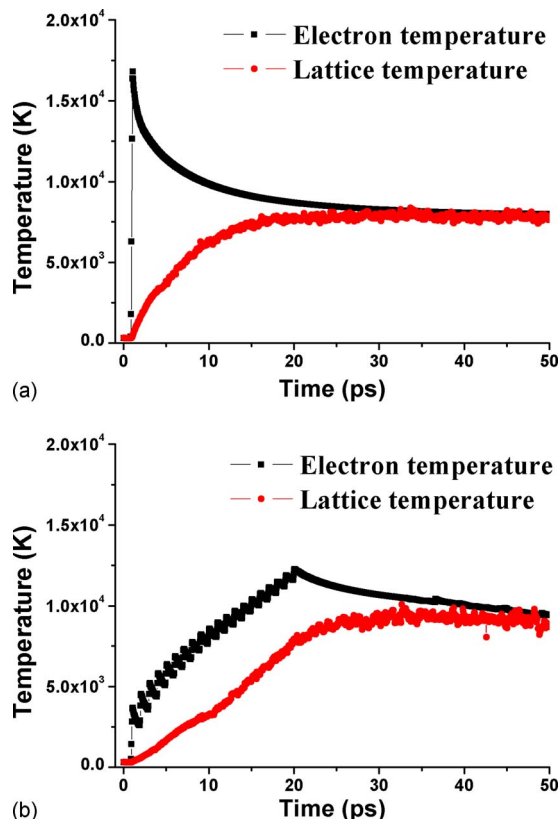

FIG. 2. (Color online) The electron and lattice temperatures of the layers next to dynamic film surfaces. (a) The single pulse case. (b) The 20 pulse case.

the maximum value of 16 800 K. The electrons and lattice reach the same temperature of 8100 K at 35 ps, which is the thermalization time defined as the characteristic time for the electrons and the lattices to reach thermal equilibrium.[28] In the 20 pulse case, the electron temperature is increased to the first peak of 3660 K by the first pulse. The electron temperature is further increased by the subsequent lasers and reaches the maximum value of 12 300 K. At 60 ps and 8800 K, the electron and lattice temperatures reach the thermalization. The pulse train technology increases the surface temperatures and prolongs the thermalization time.

Figure 3 shows the thermal conductivity of electrons of the layers next to dynamic film surfaces. In the single pulse case, the thermal conductivity can be as high as 3480 W/m K. The laser energies transfer rapidly into the thin films. In the 20 pulse case, the thermal conductivity can be increased to 980 W/m K by the first pulse and 700–140 W/m K by the subsequent pulses. The pulse train technology reduces the electron thermal conductivity dramatically due to lower single pulse fluences or higher transient surface temperatures, which ensures that the laser energies of pulse trains are mainly deposited within the nanoscale layers of the dynamic film surfaces.

Figures 4 and 5 show the lattice temperature distributions and stress distributions, respectively. Initially, the nickel thin films are equilibrated at 300 K. In the single pulse case, the temperatures of the films increase dramatically and the absorbed energies transfer rapidly into the thin films within 15 ps. After that, the surface temperature increases gradually to 8370 K. At 200 ps, the surface temperature decreases to 7600 K. Strong compressive stresses and moderate tensile stresses are generated in sequence and propagate into the thin films. Note that the tensile stress tends to decrease the film density.[26] For the high temperature liquids in melting regions, the decrease in film density will directly induce the phase separation (coexistence of liquid phase and vapor
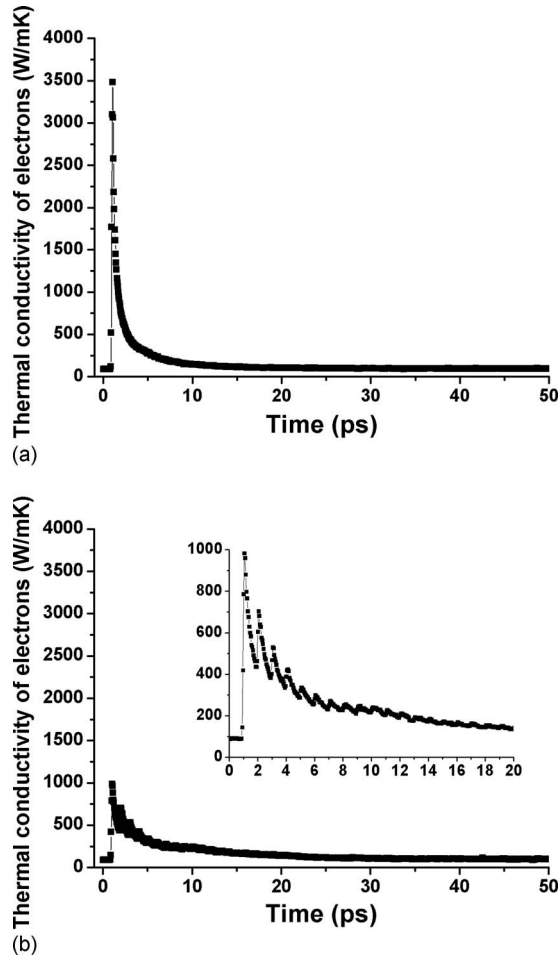
FIG. 3. The thermal conductivity of electrons of the layers next to dynamic film surfaces. (a) The single pulse case. (b) The 20 pulse case.

FIG. 4. (Color online) The lattice temperature distributions at different times. (a) The single pulse case. (b) The 20 pulse case.

phase), which is responsible for film disintegration and gas bubble generation.[26] In the 20 pulse case, the temperatures of the films increase gradually and the melting fronts (the temperature disorder positions) appear and move into the thin films at a lower propagation velocity. The subsequent pulses cause the temperatures of surface melting regions increase much faster than those of inner solid regions. This is because high temperatures of melting regions reduce the thermal conductivity of electrons, which leaves the absorbed energies mainly deposited in the dynamic film surfaces. At 32 ps, the surface temperature achieves 10 080 K (higher than the critical temperature of 9450 K[26,29]) which will directly induce the critical point phase separation. At 200 ps, the surface temperature decreases to about 7500 K. Compared with single pulse ablation at the same total fluence, the 20 pulse ablation can achieve (1) higher dynamic surface temperature during 20—145 ps, (2) lower dynamic surface temperature during 1–20 and 145—200 ps, and (3) lower bottom surface temperature during 1–200 ps, which is favorable in inducing the critical point phase separation and reducing the heat-affected zone of laser ablation at the same time. Furthermore, in the 20 pulse case, lower compressive and tensile stresses are generated in sequence by the pulse train and propagate into the thin films. Note that the lower tensile stresses can hardly
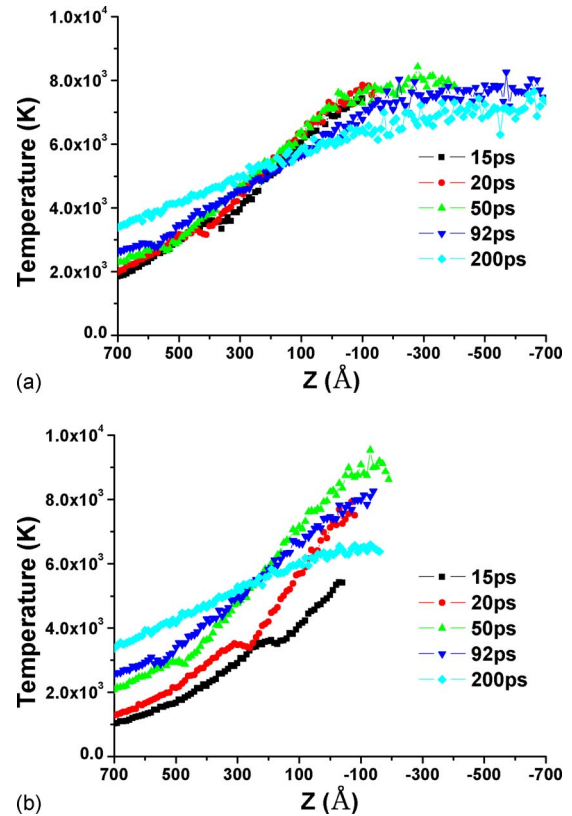
induce the liquid-vapor phase separation within inner film regions, which avoids the film disintegration and gas bubble generation.

Figure 6 shows the time evolutions of the system in the ρ-T plane for different regions. Two regions are considered, including the layers next to dynamic film surfaces and the positions of $z=-7$ nm (the time evolutions are tracked after $z=-7$ nm become subsurface film regions). Initially, for the system, density=8900 kg/m^3 and $T=300$ K. In the single pulse case, materials of dynamic film surfaces expand rapidly, which get across the binodal line and approach the spinodal line [Fig. 6(a)1]. Materials of subsurface film regions experience a rapid expansion and approach the binodal line to become metastable liquids. After that, the rapidly expanding materials approach and get across the spinodal line, which is the limit of superheating in metastable liquids.[30,31] At this time, several gas bubbles occur inside the thin films which indicate the decomposition of metastable liquids into mixtures of liquid phase and vapor phase [Fig. 6(a)2]. Here, the phase explosion is the dominant phase change mechanism. In the 20 pulse case, the absorbed energy of pulse trains is mainly deposited within the nanoscale layers of the dynamic film surfaces. Therefore, materials of dynamic film surfaces are fast heated to much higher temperatures, which ensures that the time evolutions of system are far from the metastable zones (between binodal line and spinodal line[26]) and directly achieve the supercritical state. The materials remain as high temperature and relatively homogeneous structures during the supercritical state, which help for more and smaller uniform nanoparticle generation. Then, materials of
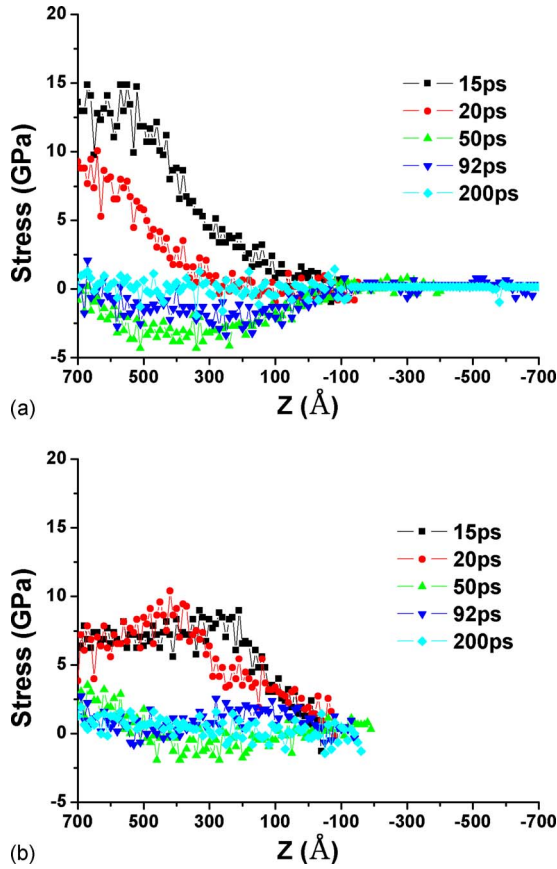
FIG. 5. (Color online) The stress distributions at different times, where the positive value denotes the compressive stress and the negative value donates the tensile stress. (a) The single pulse case. (b) The 20 pulse case.

dynamic film surfaces enter the metastable zones below the critical point and cause phase separation. Rapidly, materials of uppermost film region further transform into dense liquids. Here, the critical point phase separation is the dominant phase change mechanism [Fig. 6(b)1]. Especially, the temperatures of dynamic film surfaces are slightly above the critical point, which ensures the materials to transform rapidly from supercritical state to dense liquids. In the 20 pulse case, the temperatures of subsurface films regions are lower than critical point. The compressive stresses and tensile stresses are confined significantly which avoids the phase explosion. Materials of subsurface films regions only achieve the binodal line and show no liquid-vapor phase separation [Fig. 6(b)2]. Note that the temperatures of dynamic film surfaces are slightly above the critical point, so only nanoscale layers can achieve critical point phase separation. And the subsurface layers whose temperatures are lower than critical point will achieve no liquid-vapor phase separation due to the significant decrease in the film compressive stresses and tensile stresses. Compared with single pulse ablation at the same total fluence, the time evolutions of the system in the ρ-T plane are changed by the pulse trains: (1) within dynamic film surfaces, the critical point phase separation plays a dominant role; (2) within subsurface films regions, no liquid-vapor phase separation occurs. The critical point phase separation can induce more and smaller nanoparticle generation within the dynamic film surfaces, which is favorable for high precision of microanalysis application. No liquid-vapor
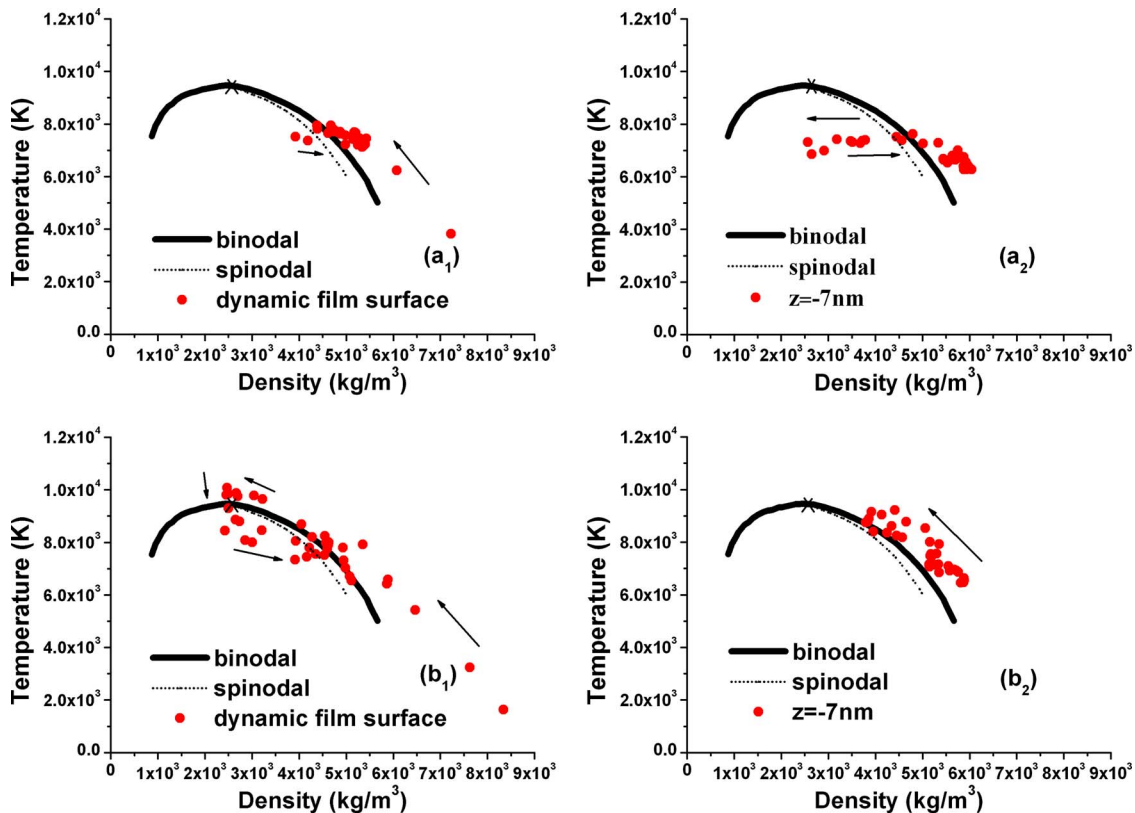

FIG. 6. (Color online) Time evolution of the system in the ρ-T plane for different regions. Solid line: binodal, dashed line: spinodal, and cross: critical point (Ref. 22). The arrows indicate the time evolution. (a) The single pulse case. (b) The 20 pulse case.

phase separation, rather than the phase explosion, occurs within subsurface film regions, which is favorable for high quality micro-/nanofabrication.

IV. CONCLUSION

MD simulations combined with TTM are employed to study the phase change mechanisms during femtosecond laser pulse train ablation of nickel thin films. The electron heating process can be changed by pulse trains to ensure that the absorbed energy of the pulse trains is mainly deposited within the nanoscale layers of the dynamic film surfaces. Furthermore, the phase change process can be changed in a way that the pulse trains reduce both the compressive and tensile stresses, and induce the critical point phase separation within the uppermost films and no liquid-vapor phase separation within the subsurface films, rather than the phase explosion, at the total laser fluence slightly above the volumetric phase change threshold fluence of single pulse ablation, which is favorable for precision fabrication and small uniform nanoparticle generation.

[1] Y. Hirayama and M. Obara, J. Appl. Phys. **97**, 064903 (2005).
[2] C. P. Grigoropoulos, D. J. Hwang, and A. Chimmalgi, MRS Bull. **32**, 16 (2007).
[3] A. Y. Vorobyev, V. S. Makin, and C. L. Guo, J. Appl. Phys. **101**, 034903 (2007).
[4] B. Rethfeld, A. Kaiser, M. Vicanek, and G. Simon, Phys. Rev. B **65**, 214303 (2002).
[5] R. Bartels, S. Backus, E. Zeek, L. Misoguti, G. Vdovin, I. P. Christov, M. M. Murnane, and H. C. Kapteyn, Nature (London) **406**, 164 (2000).
[6] A. Lindinger, C. Lupulescu, M. Plewicki, F. Vetter, A. Merli, M. S. Weber, and L. Woste, Phys. Rev. Lett. **93**, 033001 (2004).
[7] X. Wang, S. Amoruso, and J. Xia, Appl. Surf. Sci. **255**, 5211 (2009).
[8] S. Singha, Z. Hu, and R. J. Gordon, J. Appl. Phys. **104**, 113520 (2008).
[9] A. Semerok and C. Dutouquet, Thin Solid Films **453–454**, 501 (2004).
[10] S. Noël and J. Hermann, Appl. Phys. Lett. **94**, 053120 (2009).
[11] F. Korte, S. Adams, A. Egbert, C. Fallnich, A. Ostendorf, S. Nolte, M. Will, J.-P. Ruske, B. N. Chichkov, and A. Tünnermann, Opt. Express **7**, 41 (2000).
[12] H. Chen, X. Chen, Y. Zhang, and Y. Xia, Laser Phys. **17**, 1378 (2007).
[13] A. Y. Vorobyev and C. L. Guo, Phys. Rev. B **72**, 195422 (2005).
[14] L. Jiang and H. L. Tsai, Int. J. Heat Mass Transfer **50**, 3461 (2007).
[15] L. Jiang and H. L. Tsai, Appl. Phys. Lett. **87**, 151104 (2005).
[16] J. Huang, Y. Zhang, and J. K. Chen, Int. J. Heat Mass Transfer **52**, 3091 (2009).
[17] D. S. Ivanov and L. V. Zhigilei, Phys. Rev. B **68**, 064114 (2003).
[18] C. Cheng and X. Xu, Appl. Phys. A: Mater. Sci. Process. **79**, 761 (2004).
[19] X. Wang and Y. F. Lu, J. Appl. Phys. **98**, 114304 (2005).
[20] T. Q. Qiu and C. L. Tien, Int. J. Heat Mass Transfer **35**, 719 (1992).
[21] J. Hohlfeld, S. S. Wellershoff, J. Gudde, U. Conrad, V. Jahnke, and E. Matthias, Chem. Phys. **251**, 237 (2000).
[22] L. A. Girifalco and V. G. Weizer, Phys. Rev. **114**, 687 (1959).
[23] G. L. Eesley, Phys. Rev. B **33**, 2144 (1986).
[24] X. Wang, ASME J. Heat Transfer **126**, 355 (2004).
[25] C. Schafer, H. M. Urbassek, L. V. Zhigilei, and B. J. Garrison, Comput. Mater. Sci. **24**, 421 (2002).
[26] C. Cheng and X. Xu, Phys. Rev. B **72**, 165415 (2005).
[27] J. Kim, S. Na, S. Cho, W. Chang, and K. Whang, Opt. Lasers Eng. **46**, 306 (2008).
[28] L. Jiang and H. L. Tsai, ASME J. Heat Transfer **127**, 1167 (2005).
[29] D. A. Young and B. J. Alder, Phys. Rev. A **3**, 364 (1971).
[30] X. Xu, in *Annual Review of Heat Transfer*, edited by C.-L. Tien, V. Prasad, and F. P. Incropera (Bell House, New York, 2001), Vol. 12, p. 79.
[31] P. Lorazo, L. J. Lewis, and M. Meunier, Phys. Rev. Lett. **91**, 225502 (2003).